

# Bayesian Models for Deriving Biogeochemical Information from Satellite Ocean Color

**Susanne E. Craig<sup>1, 2</sup> and Erdem M. Karaköylü<sup>1, 3</sup>**

<sup>1</sup>Ocean Ecology Laboratory, NASA Goddard Space Flight Center, Greenbelt, Maryland, USA; [susanne.e.craig@nasa.gov](mailto:susanne.e.craig@nasa.gov)

<sup>2</sup>Universities Space Research Association, NASA Goddard Space Flight Center, Greenbelt, Maryland, USA

<sup>3</sup>Science Applications International Corporation, NASA Goddard Space Flight Center, Greenbelt, Maryland, USA; [jkomd.283.2112@gmail.com](mailto:jkomd.283.2112@gmail.com)

This manuscript is a non-peer reviewed preprint submitted to Earth ArXiv. Please note that this manuscript has yet to undergo peer review or to be formally accepted for publication in a peer reviewed journal. Please feel free to contact either of the authors – we welcome your feedback.

# Bayesian Models for Deriving Biogeochemical Information from Satellite Ocean Color

Susanne E. Craig<sup>1, 2</sup> and Erdem M. Karaköylü<sup>1, 3</sup>

<sup>1</sup>Ocean Ecology Laboratory, NASA Goddard Space Flight Center, Greenbelt, Maryland, USA; [susanne.e.craig@nasa.gov](mailto:susanne.e.craig@nasa.gov)

<sup>2</sup>Universities Space Research Association, NASA Goddard Space Flight Center, Greenbelt, Maryland, USA

<sup>3</sup>Science Applications International Corporation, NASA Goddard Space Flight Center, Greenbelt, Maryland, USA; [jkomd.283.2112@gmail.com](mailto:jkomd.283.2112@gmail.com)

***This paper is a non-peer reviewed preprint submitted to Earth ArXiv.***

# Bayesian Models for Deriving Biogeochemical Information from Satellite Ocean Color

Susanne E. Craig<sup>1,2</sup> and Erdem M. Karaköylü<sup>1,3</sup>

<sup>1</sup>Ocean Ecology Laboratory, NASA Goddard Space Flight Center; <sup>2</sup>Universities Space Research Association; <sup>3</sup>Science Applications International Corporation

This manuscript was compiled on November 24, 2019

biological oceanography | phytoplankton | machine learning | satellite remote sensing | atmospheric correction

1 The era of satellite ocean color began in 1978 with the  
2 launch of NASA's Coastal Ocean Color Scanner (CZCS) on  
3 board the Nimbus-7 spacecraft. Through measurement of the  
4 quantity and quality of the light reflected from the ocean,  
5 CZCS revolutionized our understanding of the intimate re-  
6 lationships between ocean physics and phytoplankton distri-  
7 bution in the world ocean (1). Generations of spaceborne  
8 sensors have subsequently followed, and satellite ocean color  
9 measurements now provide spatial and temporal distributions  
10 of phytoplankton (2) and other aquatic biogeochemical  
11 constituents (3), estimates of ocean primary productivity (4, 5),  
12 and have become a vital input to global models of Earth  
13 system processes and their response to a changing climate  
14 (6, 7).

15 Ocean color is derived from the signal collected at the top  
16 of the atmosphere (TOA) by a satellite spectroradiometer.  
17 The majority of this signal is due to scattering from atmo-  
18 spheric aerosols and reflection by wind-generated whitecaps,  
19 with only ~10% maximum of the spectrum due to radiance  
20 either reflected from the ocean surface or scattered back out  
21 through the air-water interface. The atmospheric contribution  
22 must, therefore, be 'subtracted' from the TOA signal in order  
23 to derive the oceanic contribution. This is achieved opera-  
24 tionally through the process of atmospheric correction (AC),  
25 which removes the influence of sun glint, whitecaps formed  
26 by wind, and the contribution by atmospheric aerosols. This  
27 latter step takes advantage of the fact that the water body  
28 can be considered to be totally absorbing (i.e. black) in the  
29 near infrared (NIR). Any TOA signal detected at wavelengths  
30 in the NIR is then attributed to atmospheric contributions  
31 and a suitable aerosol radiance model is chosen to extrapolate  
32 to shorter wavelengths. This derived atmospheric radiance  
33 is subtracted from the total TOA spectrum, and the signal  
34 that remains is the water-leaving radiance. Remote sensing  
35 reflectance ( $R_{rs}$ ,  $sr^{-1}$ ) i.e. the light exiting the water normal-  
36 ized to a hypothetical condition of an overhead Sun and no  
37 atmosphere (8, 9), can then be calculated. Following calcu-  
38 lation of  $R_{rs}$ , various approaches are used to estimate water  
39 constituent concentrations. These fall broadly into two classes  
40 of algorithms: i) empirical band-ratio algorithms, which are  
41 derived from the statistical relationship between the ratio of  
42 two or more wavebands (blue and green) of  $R_{rs}$  and *in situ*  
43 measurements of chlorophyll a concentration, Chl a ( $mg\ m^{-3}$ ),  
44 a proxy for phytoplankton biomass (2), and ii) semi-analytical

45 algorithms that are based on a combination of radiative trans-  
46 fer theory and empirically derived parameters, and that permit  
47 the retrieval of inherent optical properties (IOPs) such as spec-  
48 tral particulate backscattering,  $b_{bp}$  ( $m^{-1}$ ), and phytoplankton  
49 absorption,  $a_{ph}$  ( $m^{-1}$ ), coefficients that can be related to the  
50 water constituents of interest (3).

51 In a very general sense, AC approaches perform well over  
52 the open ocean where the water is totally absorbing in the  
53 NIR and the aerosol assemblage can be well modeled. How-  
54 ever, AC performance becomes severely limited in coastal and  
55 inland waters where bottom reflectance can contaminate water-  
56 leaving signals, suspended sediments may produce a non-zero  
57 reflectance in the NIR, and/or absorbing aerosols, e.g. those  
58 generated by terrestrial anthropogenic sources (10), are dif-  
59 ficult to model accurately. The performance of the in-water  
60 algorithms is also degraded in these regions for a variety of  
61 reasons. The band ratio algorithms were developed for use in  
62 case 1 waters, i.e. those in which ocean color is dominated by  
63 Chl a and all other optically active water constituents covary  
64 (11). In case 2 waters (11), where other optically active water  
65 constituents vary independently of Chl a (e.g. coastal waters),  
66 band ratio algorithms often perform poorly as colored dissolved  
67 organic material (CDOM) and suspended particulate material  
68 compete with phytoplankton for the absorption and scattering  
69 of blue photons, thereby confounding the algorithm's assump-  
70 tion of co-variability. Semi-analytical models may perform  
71 satisfactorily in case 2 waters, but model parameters such as  
72 the spectral slopes of CDOM+detrital absorption and particu-  
73 late backscattering may need to be regionally tuned as their  
74 local values can vary widely (12-14). Additionally, the signal  
75 of interest may simply be swamped by competing processes – a  
76 common occurrence in case 2 waters where CDOM absorption  
77 coefficients can be an order of magnitude or greater than that  
78 of phytoplankton (15, 16). Finally, if AC is inaccurate, the  
79 spectral shape of the retrieved  $R_{rs}$  spectrum may be distorted,  
80 meaning that the starting point for any of these ocean color  
81 models will be fundamentally flawed. As a result of these  
82 challenges, satellite measurements made over such water bod-  
83 ies are often unusable for quantitative studies. The loss of  
84 information from these systems is particularly egregious as  
85 they are vulnerable to climate and anthropogenic forcing (17),  
86 play host to highly productive fisheries (18), or are regions  
87 of intense atmospheric  $CO_2$  uptake (19) or sinking of organic  
88 matter for climate-relevant time scales (20, 21).

89 Work has been devoted to improving the standard AC and  
90 a number of alternative approaches have been proposed (22).  
91 These include a multiband AC that uses multiple NIR and  
92 shortwave infrared channels (23), and several neural network  
93 (NN) techniques that provide a universal method to approxi-  
94 mate arbitrary non-linear functions. The NNs are used to solve  
95 the AC problem directly (i.e. inputs of observed reflectance  
96 and viewing geometry and water reflectance as output), or to  
97 model the radiative transfer equation (RTE) itself, thereby  
98 saving the substantial computational time taken to solve the  
99 RTE (see Frouin et al. (22) and references therein). In a  
100 similar vein, a number of in-water studies have investigated  
101 similar approaches using NNs to estimate Chl, IOPs, apparent  
102 optical properties (AOPs) and water constituent concentra-  
103 tions for optically complex (i.e. case 2) waters (24–28). Craig  
104 et al. (16) developed a method based on empirical orthogonal  
105 function (EOF) analysis of hyperspectral  $R_{rs}$  to estimate IOPs  
106 in an optically complex water body, then further developed  
107 the technique to estimate IOPs directly from TOA reflectance  
108 spectra, thereby combining AC with in-water IOP estimation  
109 [ref]. Collectively, these approaches present an alternative  
110 paradigm for retrieving biogeochemically relevant information  
111 from ocean color, particularly in scenarios where it may other-  
112 wise not be possible. However, ocean color science has yet to  
113 fully embrace the potential of these approaches, in particular  
114 machine learning, which has undergone rapid development  
115 and democratization. Several source codes are now available  
116 via open source platforms, and ML is used routinely and oper-  
117 ationally in many of the Earth sciences, e.g. in meteorology  
118 (29) or plankton taxonomic studies (30), where the abundance  
119 of data enables the use of state-of-the art approaches such  
120 as deep learning. Ocean color remote sensing, on the other  
121 hand, suffers from a severe lack of labelled data (3), i.e. in situ  
122 observations that can be matched with satellite observations,  
123 and this reduces the number of approaches that can be used  
124 in a principled way to estimate IOPs and their uncertainty.  
125 Moreover, this labelled data is inherently noisy due to factors  
126 such as environmental fluctuations, measurement error, and  
127 sensor uncertainty. These obstacles make the development of  
128 generalizable models (i.e. models that capture the signal but  
129 not the noise in training data) very challenging. To address  
130 these issues, we use a Bayesian approach(31, 32) in developing  
131 our models. We chose this approach because the inclusion  
132 of sufficiently informed prior information can guard against  
133 overfitting, while providing transparency with respect to mod-  
134 eling assumptions. Furthermore, estimates of modeling and  
135 prediction uncertainty are the default of Bayesian models. Un-  
136 like frequentist concepts such as the p-value and confidence  
137 intervals, Bayesian credibility intervals derived from model  
138 posterior distributions are unambiguous and can be readily  
139 interpreted(33, 34).

140 Here, we present a machine learning effort that extends  
141 the previous work of Craig (35) by using TOA reflectance in  
142 Bayesian predictive models of the phytoplankton absorption  
143 coefficient,  $a_{ph}$ .  $a_{ph}$  is an information-rich parameter that  
144 can provide an alternative proxy of phytoplankton biomass  
145 (36), insight into community composition (37, 38), and can  
146 quantify the light available for photosynthesis in primary pro-  
147 duction models, making it an ideal candidate for use as an  
148 Essential Climate Variable (39) or Essential Ocean Variable  
149 (40). The ability to reliably estimate  $a_{ph}$  while bypassing the

150 considerable challenges of conventional AC in these ecologi-  
151 cally and economically important waters provides a significant  
152 advancement of our fundamental understanding of biogeochem-  
153 ical processes, and the insight required to effect meaningful  
154 ecosystem management and climate change mitigation strate-  
155 gies.

## 156 Results

157 Three hierarchical Bayesian models predicting phytoplankton  
158 absorption at 6 wavebands were successfully fitted. In increas-  
159 ing order of complexity, these models were linear regression,  
160 linear regression with first order interaction terms, and neural  
161 network. Input variables included 6 principal components de-  
162 rived from 6 Rayleigh-corrected bands, in addition to a number  
163 of ancillary predictors (see Materials and Methods section).  
164 All three models were built to highlight predictor relevance.  
165 This is depicted in order of relevance for each model in the  
166 forest plots shown in Fig. 1 for phytoplankton absorption at  
167 411 nm,  $a_{ph}(411)$ . Note that we use  $a_{ph}(411)$  in Fig. 1 as an  
168 illustrative example because this region of the spectrum is typi-  
169 cally the most affected by inaccurate atmospheric correction  
170 and, therefore, represents the most challenging scenario for  
171 ocean color retrievals. For all models, the first three principal  
172 components appear among the more influential variables. The  
173 linear regression model identified sea surface temperature and  
174 bathymetry ( $sst$  and  $dep$  in Fig. 1, top panel) as significantly  
175 relevant in predicting  $a_{ph}(411)$ . For the linear regression with  
176 interaction model, interaction between the first two spectral  
177 principal components ( $pc1$  and  $pc2$ ), and interaction between  
178 the fourth principal component and the solar zenith angle ( $pc4$   
179 and  $solz$ ) were found to be the most influential variables (Fig.  
180 1, middle panel). Interestingly, the neural network deemed  
181 only PC spectral information as relevant in  $a_{ph}(411)$  prediction  
182 (Fig. 1, bottom panel).

183 The uncertainties around the relevant parameters were  
184 similar in magnitude between the two types of linear regression  
185 models. In the case of the neural network, the most relevant  
186 parameters exhibit the greatest uncertainty (Fig. 1, bottom  
187 panel), likely an effect of the small size of the data set used.  
188 This pattern changes, however, where model prediction skill  
189 is concerned. To assess each model’s prediction skill, a small  
190 out-of-sample data set was used and the following criteria  
191 examined: 1) how tight the 95% credibility interval of the  
192 posterior predictive simulation was (Fig. 2); 2) where out-  
193 of-sample observations occur in relation to the 95% and 50%  
194 credibility intervals (Fig. 2); and 3) how closely average  
195 predictions tracked out-of-sample observations (Figs. 2 - 5).

196 We found that for all bands, and for all performance criteria  
197 listed above, expected predictive performance on out-of-sample  
198 data (i.e. future, unseen data) increased with model complex-  
199 ity. Linear regression was the least proficient of the three  
200 models, while the Bayesian neural network was the model  
201 most likely to generalize well. Of all 6 bands tested,  $a_{ph}(555)$   
202 was the most challenging to fit across all models, likely due to  
203 the fact that phytoplankton absorption is weakest in the green  
204 spectral region. This behavior was also observed by Craig et  
205 al.(16) in their PC-based models.

## 206 Discussion

207 This study clearly illustrates the feasibility of retrieving  
208 the spectral phytoplankton absorption coefficient from op-

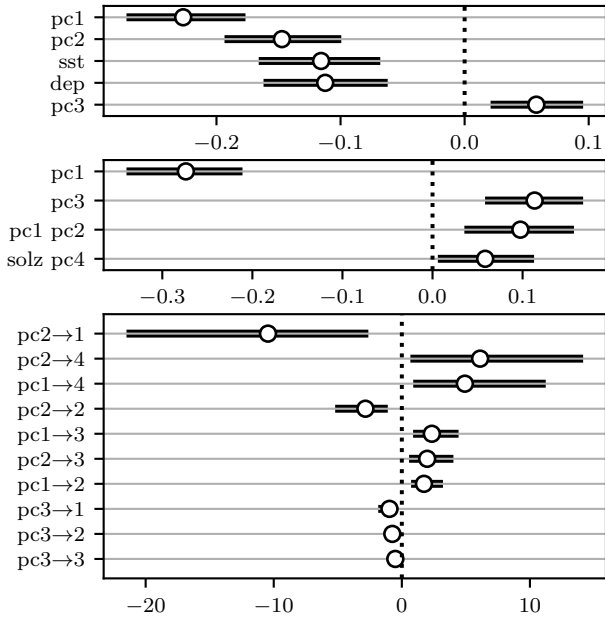


**Fig. 1.** Forest plots for 3 Bayesian models of  $a_{ph}(411)$ ; **top** - linear regression; **middle** - linear regression with interactions; **bottom** - neural network. Open circles and whiskers are mean and 95% credibility intervals (CI), respectively, for model coefficients. Each coefficient (shown on the left axes) corresponds to a predictor variable. For brevity, only the most significant predictors (i.e. their CIs do not overlap the vertical dotted zero line) are shown here in order of descending significance. Predictor abbreviations area as follows; *pc* - principal component, *sst* - sea surface temperature, *dep* - depth, *solz* - solar zenith angle. Interaction (middle panel) is shown as two predictors side by side. Bottom panel shows predictor connection to neural network hidden layer unit.

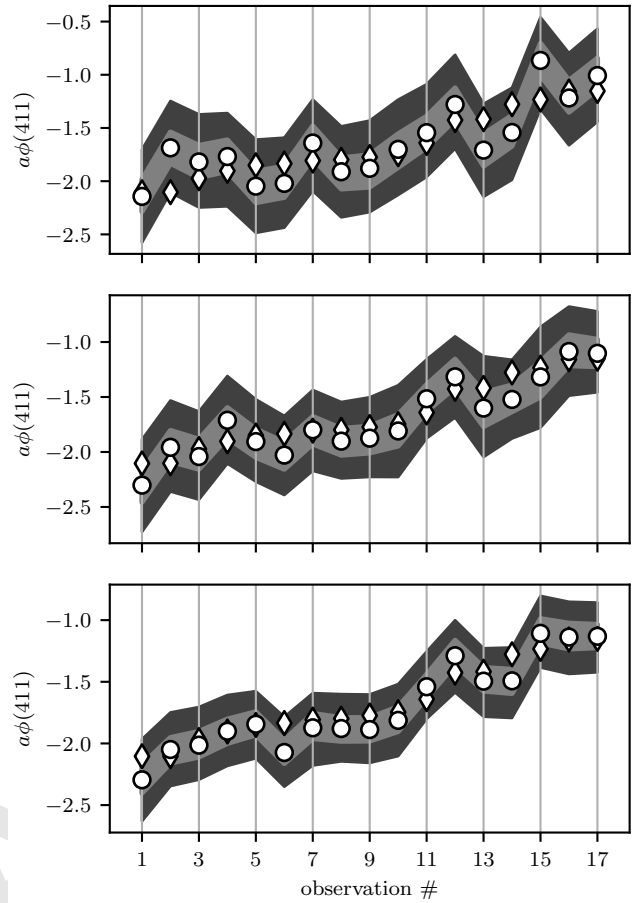


**Fig. 2.** Posterior predictive plots of out-of-sample  $a_{ph}(411)$  data for linear regression (**top**), linear regression with interaction (**middle**), neural network (**bottom**). Y-axes are log scaled. Open diamond  $\rightarrow$  out-of-sample observation, arranged monotonically in ascending order; open circle  $\rightarrow$  mean model prediction; light gray envelope  $\rightarrow$  50% credibility interval (CI); dark gray envelope  $\rightarrow$  95% CI.

209 tically complex coastal waters using Rayleigh-corrected Top-  
 210 of-Atmosphere reflectance as principal input to a number of  
 211 models. Of these, Bayesian neural networks resulted in the  
 212 most robust predictions. This is of particular significance as  
 213 the information contained in remotely sensed signals of such  
 214 waters is often irretrievably lost due to failure of atmospheric  
 215 correction and/or retrieval algorithms. To date, Bayesian ap-  
 216 proaches have not been used for information retrieval from  
 217 ocean color and offer a viable alternative to traditional ra-  
 218 diative transfer and semi-analytical models. Additionally,  
 219 Bayesian models provide uncertainty estimates due to their  
 220 probabilistic nature - something that must be done *post hoc*  
 221 if using conventional approaches. The Bayesian framework  
 222 allows all information concerning uncertainty to be included  
 223 via formulation of the prior distributions - i.e. environmental,  
 224 instrumental, systematic uncertainty can all be included in  
 225 the model if that information is available. This provides a  
 226 fundamental improvement in how ocean color signals can be  
 227 used to robustly describe highly dynamic aquatic ecosystems.

228 Another important feature of this approach is the ability  
 229 to bypass conventional atmospheric correction techniques. In  
 230 coastal, inland waters and other optically complex scenarios,  
 231 it is challenging to accurately achieve atmospheric correction  
 232 due to the complex assemblage of aerosols that must be mod-  
 233 eled and/or the non-zero water leaving radiance that violates  
 234 fundamental AC model assumptions. In this approach, we  
 235 do not attempt to subtract the atmospheric contribution, but  
 236 instead use principal component analysis to 'tease out' the

237 lower modes of variance underlying the large atmospheric sig-  
 238 nal detected by the satellite sensor. In so doing, we assume  
 239 nothing regarding the atmospheric scattering and absorbing  
 240 properties and simply allow the orthogonality conditions of  
 241 PCA to detect the underlying signals associated with the water  
 242 and its constituents. Traditional approaches for AC in opti-  
 243 cally complex waters typically struggle with negative water  
 244 leaving radiances at the blue end of the spectrum, i.e. too  
 245 much radiance at the blue end of the spectrum is attributed  
 246 to the atmosphere by the models used, resulting in a non-  
 247 physical, negative water-leaving signal. Our approach is able  
 248 to completely circumvent this problem and retrieve  $a_{ph}(\lambda)$   
 249 in the blue with high accuracy.

## Materials and methods

250 **Data collection.** A modified version of the NOMAD  
 251 (Werdell and Bailey 2005) SeaWiFS satellite-to-in situ  
 252 validation dataset was used for model development  
 253 (<http://seabass.gsfc.nasa.gov/>). This was comprised of a sub-  
 254 set of the NOMAD dataset limited to stations with coincident  
 255 and valid SeaWiFS coverage (Fig. 6), and included  $R_{rs}$  and  
 256 TOA radiance ( $L_t(\lambda)$ ;  $\mu W cm^{-2} nm^{-1} sr^{-1}$ ) in addition to  
 257

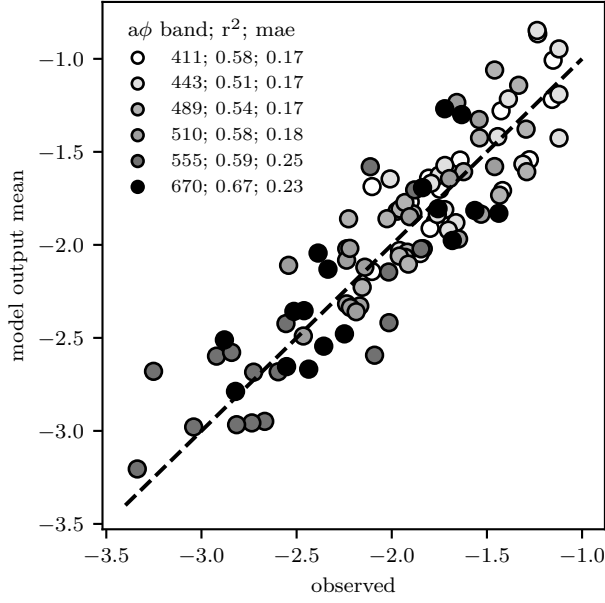


Fig. 3. Out-of-sample observed vs. prediction mean from linear regression for  $a_\phi$  at 6 bands, featuring  $r^2$  and mean absolute error (mae) as goodness-of-fit measures. Both axes are log-scaled

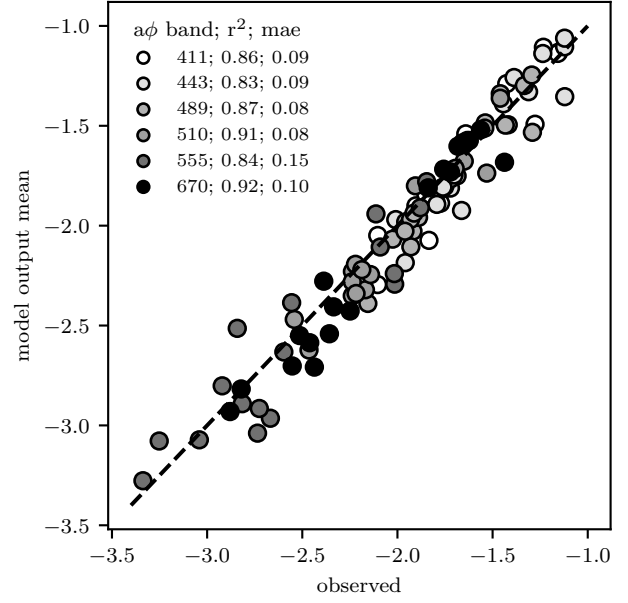


Fig. 5. Out-of-sample observed vs. prediction mean from neural network with interactions for  $a_\phi$  at 6 bands, featuring  $r^2$  and mean absolute error (mae) as goodness-of-fit measures. Both axes are log-scaled

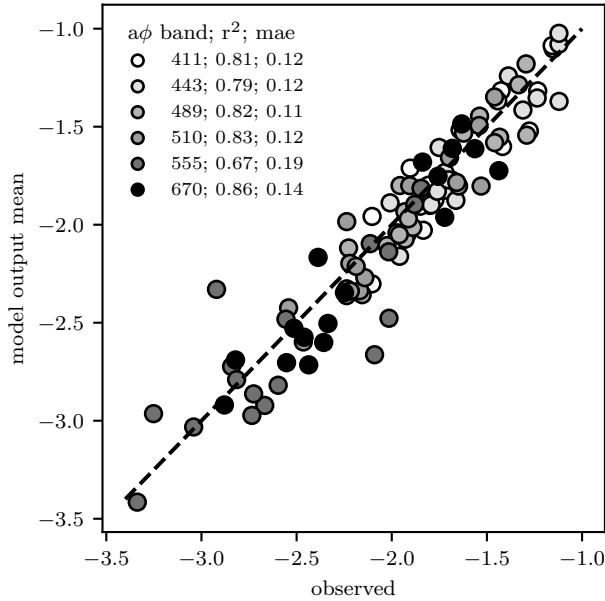


Fig. 4. Out-of-sample observed vs. prediction mean from linear regression with interactions for  $a_\phi$  at 6 bands, featuring  $r^2$  and mean absolute error (mae) as goodness-of-fit measures. Both axes are log-scaled

$$R_{rc}(\lambda) = \frac{L_t(\lambda) - L_r(\lambda)}{F_0 \cos(\theta_0) t t_0} \quad [1] \quad 263$$

where  $L_r$  is the Rayleigh scattering radiance (264  $\mu W cm^{-2} nm^{-1} sr^{-1}$ ),  $F_0$  the extraterrestrial solar irradiance (265  $\mu W cm^{-2} nm^{-1}$ ),  $\theta_0$  is the solar zenith angle (degrees), (266  $t$  the diffuse transmittance from the satellite pixel to the satellite (dimensionless) and  $t_0$  the diffuse transmittance from the sun to the pixel (dimensionless). (267 268 269

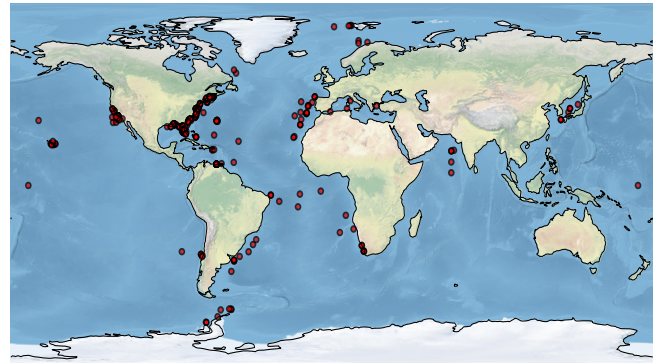


Fig. 6. In-situ sampling stations used in this study.

**Data pre-processing.** The NOMAD *in situ*  $a_{ph}(\lambda)$  data was (270 provided at 20 wavelengths. This was reduced to 6 to match (271 SeaWiFS visible wavelengths of 412, 443, 490, 510, 555, 670 (272 nm. Data points were discarded if no *in situ*  $a_{ph}(\lambda)$  data (273 existed or had missing wavelengths, and if any of the satellite (274 wavelengths were missing or contained zero values. Three additional (275 pre-processing steps were performed: i) The principal (276

the standard NOMAD parameters such as location, sea surface (258 temperature, water column depth, and solar zenith angle. (259 Rayleigh-corrected remote sensing reflectance ( $R_{rc}$ ;  $sr^{-1}$ ) was (260 derived using SeaDAS (version 6.2) assuming no aerosol, and (261 is given by: (262

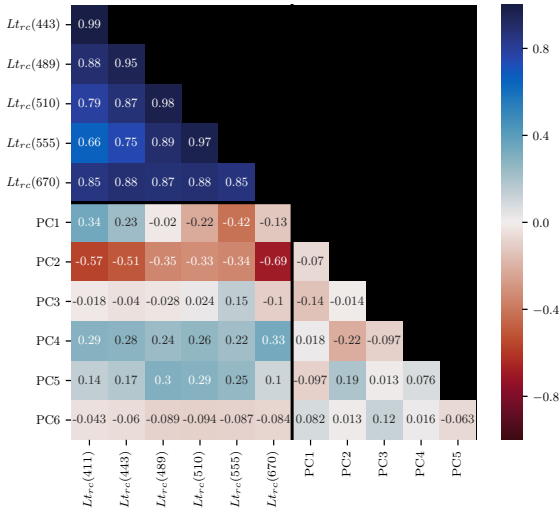


Fig. 7. Pairwise correlation heatmap. Top left quadrant suggests the multicollinearity within TOA radiances ( $L_t$ ), bottom left quadrant illustrates the link between radiances and principal components.

components (PCs) of the 6 Rayleigh-corrected remote sensing reflectances were computed. After initial model trials, it was found that the PCs were consistently more powerful predictors than the parent reflectance spectra, in agreement with the findings of Craig et al. (16) who observed that  $R_{rs}$  PCs were more important predictors of IOPs than reflectance. Using the PCs also has the advantage of eliminating the multicollinearity that exists between the reflectance wavebands (see Fig. 7). This is desirable since inclusion of multiple predictor variables that carry redundant information can introduce model non-identifiability - i.e. the inability to distinguish amongst explanations - that manifests itself by an apparent lack or weak relationship between predictors and predicted variables, when in fact the relationship is much stronger. ii) The data, which included sea surface temperature, solar zenith angle, and reflectance principal components, span widely varying scales. Therefore, they were standardized by subtracting the mean from each predictor variable and dividing by its respective standard deviation. iii) The data was split into training and testing sets, with the training set used for model fitting, while the testing (i.e., out-of-sample) set was used for model predictive skill evaluation.

**Model development and fitting.** All models described were developed in the Python language using the probabilistic programming library PyMC3(41). Bayesian models to predict the spectral phytoplankton absorption coefficient,  $a_{ph}(\lambda)$ , were developed. By definition, Bayesian model parameters and their resulting predictions are probabilistic in nature. In brief, Bayes' rule provides a way to update beliefs based on the arrival of new, relevant pieces of evidence, and is expressed as:

$$P(A|B) = \frac{P(B|A)P(A)}{P(B)} \quad [2]$$

where  $A$  is the event we want the probability of, and  $B$  is the new evidence that is related to  $A$  in some way.  $P(A|B)$  is the posterior; this is what we are estimating.  $P(B|A)$  is referred

to as the likelihood, and is the probability of observing the new evidence, given our initial hypothesis.  $P(A)$  is the prior, i.e. the probability of the hypothesis without any additional prior information.  $P(B)$  is called the marginal likelihood and is the total probability of observing the evidence.

Each model parameter is initially assigned a prior probability distribution,  $P(A)$ . The parameter space is then sampled and the likelihood of each observation conditioned on the parameter values is computed at each iteration. Using Bayes' rule, the priors are combined with the likelihood to yield a posterior distribution, which quantifies the model parameters' probability given the observations used during sampling. These priors are then updated as the model is confronted with data, through the computation of the model's likelihood for each observation as the parameter space is sampled.

We developed three Bayesian models: linear regression, linear regression with first degree feature interaction terms, and a neural network. Because it was not expected that all predictor variables would be relevant in predicting  $a_{ph}$ , all models were designed to identify predictor variables that had the greatest impact on the fit. In the case of the linear regression models, this was achieved using a regularized horseshoe prior(42). Regularized horseshoe priors are so called because of the horseshoe shape of the distribution. This shape results from the assignment of high probability both around 0 and far from 0, and low probability for intermediate values. The assignment of high probability near 0 is not unlike other sparse (where only a subset of predictors is relevant) regression model priors such as those used in Bayesian Lasso and Ridge regression models, in that they assume a number of the the model parameters will effectively shrink to 0. The horseshoe prior holds a significant advantage over Lasso or Ridge regression priors in that it assigns high probability to 0 while providing a thick tail, which reduces bias. The regularized horseshoe has the advantage that it provides a way to adjust the shrinking rate of non-zero parameters, thereby preventing the model from overfitting on the features corresponding to these non-zero parameters. Fig. 8 (top panel) shows the structure of the linear regression models, with a common intercept parameter given a Gaussian prior, the predictor slope parameters are also Gaussians with the scale parameter  $\sigma_\beta$  inherited from a combination of 3 hyperpriors (a hyperprior is an assumption made about a parameter in a prior probability assumption) as specified in (42). The linear regression equation is used as the mean of a Gaussian likelihood, which has a standard deviation with a half-Cauchy prior.

Similarly, the Bayesian neural network's construction features automatic relevance determination (ARD)(43). The neural network is fully connected and features one hidden layer. The weights between the input layer and the hidden layer have Gaussian priors as in the linear regression models. However, the spreads of priors for the weights corresponding to each predictor variable have independent half-Cauchy hyper-priors; this is the basis for ARD. On the other hand, the weights connecting the hidden layer to the output layer have Gaussian priors with a common hyperprior for their spread. The Bayesian neural network's architecture is depicted in Fig. 8, bottom panel.

All models were fit using the No U-Turn Sampler, a variant of Hamiltonian Monte-Carlo (44). For the regression models, 2000 samples were drawn after a tuning period made up of

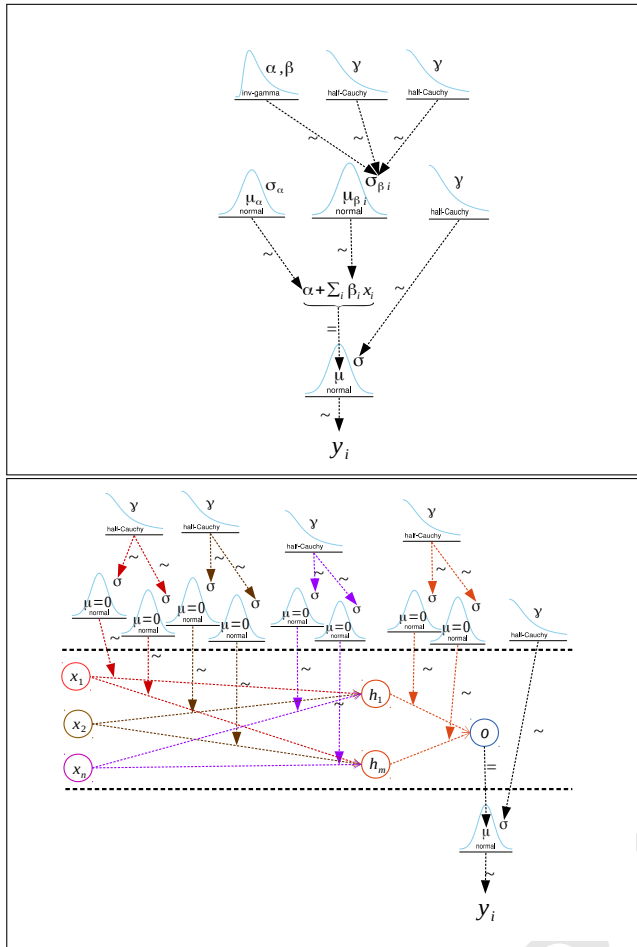


**Fig. 8.** Inference diagram of Bayesian models used. Horizontal lines separate three conceptual groups; top → priors, middle → likelihood, bottom → outcome distribution. **Top:** Regression with horseshoe priors (Models 1 & 2). **Bottom:** Bayesian neural network (Model 3). Models shown here are hierarchical, built for automatic feature relevance determination.

exchangeability problem.

**Reproducibility.** The code describing the preparation and transformation of data, as well as the code for the development, fitting, and evaluation of the models are available through github <https://github.com/madHatter106/Bayesian-ML-4-IOP-from-TOA>. The raw data is available through our project page on the Open Science Foundation website *OSF link*.

## Acknowledgments

## References

- Hovis WA, et al. (1980) Nimbus-7 coastal zone color scanner: System description and initial imagery. *Science* 210(4465):60–63.
- O'Reilly JE, Werdell PJ (2019) Chlorophyll algorithms for ocean color sensors - OC4, OC5 & OC6. *Remote Sensing of Environment* 229:32–47.
- Werdell P, et al. (2018) An overview of approaches and challenges for retrieving marine inherent optical properties from ocean color remote sensing. *Progress in Oceanography* 160:186–212.
- Behrenfeld MJ, et al. (2006) Climate-driven trends in contemporary ocean productivity. *Nature* 444:752–755.
- Saba VS, et al. (2011) An evaluation of ocean color model estimates of marine primary productivity in coastal and pelagic regions across the globe. *Biogeosciences* 8(2):489–503.
- Rousseaux CS, Gregg WW (2015) Recent decadal trends in global phytoplankton composition. *Global Biogeochemical Cycles* 29(10):1674–1688.
- Dutkiewicz S, et al. (2019) Ocean colour signature of climate change. *Nature Communications* 10(1):578.
- Gordon HR, Clark DK (1980) Remote sensing optical properties of a stratified ocean: an improved interpretation. *Appl. Opt.* 19(20):3428–3430.
- Gordon HR, Wang M (1994) Retrieval of water-leaving radiance and aerosol optical thickness over the oceans with SeaWiFS: a preliminary algorithm. *Appl. Opt.* 33(3):443–452.
- Gordon HR, Du T, Zhang T (1997) Remote sensing of ocean color and aerosol properties: resolving the issue of aerosol absorption. *Applied Optics* 36(33):8670.
- Morel A, Prieur L (1977) Analysis of variations in ocean color. *Limnology and Oceanography* 22(4):709–722.
- Craig S, et al. (2006) Use of hyperspectral remote sensing reflectance for detection and assessment of the harmful alga, *Karenia brevis*. *Applied Optics* 45(21):5414–5425.
- Darecki M, Stramski D (2004) An evaluation of MODIS and SeaWiFS bio-optical algorithms in the Baltic Sea. *Remote Sensing of the Environment* 89:326–350.
- Hu C, et al. (2003) Comparison of ship and satellite bio-optical measurements on the continental margin of the NE Gulf of Mexico. *International Journal of Remote Sensing* 24(13):2597.
- Mouw C, et al. (2015) Aquatic color radiometry remote sensing of coastal and inland waters: Challenges and recommendations for future satellite missions. *Remote Sensing of Environment* 160(0):15–30.
- Craig SE, et al. (2012) Deriving optical metrics of coastal phytoplankton biomass from ocean colour. *Remote Sensing of Environment* 119:72–83.
- Breitbart D, et al. (2018) Declining oxygen in the global ocean and coastal waters. *Science* 359(6371):eaam7240.
- Hare JA, et al. (2016) A vulnerability assessment of fish and invertebrates to climate change on the northeast u.s. continental shelf. *PLoS ONE* 11(2).
- Bauer JE, et al. (2013) The changing carbon cycle of the coastal ocean. *Nature* 504(7478):61–70.
- Mendonça R, et al. (2017) Organic carbon burial in global lakes and reservoirs. *Nature Communications* 8(1):1694.
- Bianchi TS, et al. (2018) Centers of organic carbon burial and oxidation at the land-ocean interface. *Organic Geochemistry* 115:138–155.
- Frouin RJ, et al. (2019) Atmospheric correction of satellite ocean-color imagery during the pace era. *Frontiers in Earth Science* 7:145.
- Ibrahim A, Franz BA, Ahmad Z, Bailey SW (2019) Multiband Atmospheric Correction Algorithm for Ocean Color Retrievals. *Frontiers in Earth Science* 7(116).
- Chen J, Cui T, Ishizaka J, Lin C (2014) A neural network model for remote sensing of diffuse attenuation coefficient in global oceanic and coastal waters: Exemplifying the applicability of the model to the coastal regions in Eastern China Seas. *Remote Sensing of Environment* 148:168–177.
- D'Alimonte D, Zibordi G, Berthon JF, Canuti E, Kajiyama T (2012) Performance and applicability of bio-optical algorithms in different European seas. *Remote Sensing of Environment* 124:402–412.
- Doerffer R, Schiller H (2007) The MERIS Case 2 water algorithm. *International Journal of Remote Sensing* 28(3/4):517–535.
- Tanaka A, et al. (2004) Development of a neural network algorithm for retrieving concentrations of chlorophyll, suspended matter and yellow substance from radiance data of the ocean color and temperature scanner. *Journal of Oceanography* 60(3):519–530.
- Chen J, Quan W, Cui T, Song Q, Lin C (2014) Remote sensing of absorption and scattering coefficient using neural network model: Development, validation, and application. *Remote Sensing of Environment* 149:213–226.
- Liu Y, et al. (2016) Application of deep convolutional neural networks for detecting extreme weather in climate datasets. *CoRR* abs/1605.01156.
- Ellen JS, Graff CA, Ohman MD (2019) Improving plankton image classification using context metadata. *Limnology and Oceanography: Methods* 17(8):439–461.

2000 preliminary samples that were subsequently discarded. A similar fitting procedure was followed for the Bayesian neural network, with the difference that 2000 samples were collected after a 15000-iteration tuning step. In all cases, the sampling was performed four times concurrently, but independently, to ensure convergence. The Gelman-Rubin statistic (45) was used to verify that convergence was equivalent between independent sampling runs. Relatively naive priors were used, codifying the rather loose constraint that reasonable values of the target variable would remain highly probable. An additional constraint was applied to the Bayesian neural network to address the problem of weight space symmetry (46), which affects the weights applied to the input nodes, represented as edges connecting input nodes  $x_{1...n}$  to hidden layer nodes  $h_{1...m}$  as shown in the bottom panel of Fig. 8. The problem arises from the fact that, without an additional constraint, there is nothing to differentiate hidden layer nodes from one another. In practice this results in the sampler encountering difficulty in converging on the same mode for the affected weights. The constraint applied consists of enforcing a numerical order within the weights applied to each input node. This guarantees that no overlap can occur, thus eliminating the



- 471 31. Gelman A, et al. (2013) *Bayesian Data Analysis, Third Edition*, Chapman & Hall/CRC Texts  
472 in Statistical Science. (Taylor & Francis).
- 473 32. McElreath R (2016) *Statistical Rethinking: A Bayesian Course with Examples in R and Stan*,  
474 Chapman & Hall/CRC Texts in Statistical Science. (CRC Press).
- 475 33. Kruschke JK (2015) Chapter 11 - null hypothesis significance testing in *Doing Bayesian Data*  
476 *Analysis (Second Edition)*, ed. Kruschke JK. (Academic Press, Boston), Second edition  
477 edition, pp. 297 – 333.
- 478 34. Kruschke JK (2015) Chapter 12 - bayesian approaches to testing a point ("null") hypothesis in  
479 *Doing Bayesian Data Analysis (Second Edition)*, ed. Kruschke JK. (Academic Press, Boston),  
480 Second edition edition, pp. 335 – 358.
- 481 35. Craig SE (year?) Derivation of inherent optical properties from satellite top of atmosphere  
482 measurements in optically complex waters in *NASA PACE Annual Science Team Meeting*.
- 483 36. Roesler CS, Barnard AH (2013) Optical proxy for phytoplankton biomass in the absence of  
484 photophysiology: Rethinking the absorption line height. *Methods in Oceanography* 7(0):79–  
485 94.
- 486 37. Uitz J, Stramski D, Reynolds RA, Dubranna J (2015) Assessing phytoplankton community  
487 composition from hyperspectral measurements of phytoplankton absorption coefficient and  
488 remote-sensing reflectance in open-ocean environments. *Remote Sensing of Environment*  
489 171:58–74.
- 490 38. Ciotti AM, Lewis MR, Cullen JJ (2002) Assessment of the relationships between dominant  
491 cell size in natural phytoplankton communities and the spectral shape of the absorption coef-  
492 ficient. *Limnology and Oceanography* 47(2):404–417.
- 493 39. Bojinski S, et al. (2014) The concept of essential climate variables in support of climate re-  
494 search, applications, and policy. *Bulletin of the American Meteorological Society* 95(9):1431–  
495 1443.
- 496 40. Miloslavich P, et al. (2018) Essential ocean variables for global sustained observations of  
497 biodiversity and ecosystem changes. *Global Change Biology* 24(6):2416–2433.
- 498 41. Salvatier J, Wiecki TV, Fonnesbeck C (2016) Probabilistic programming in python using  
499 PyMC3. *PeerJ Computer Science* 2:e55.
- 500 42. Piironen J, Vehtari A (2017) Sparsity information and regularization in the horseshoe and  
501 other shrinkage priors. *ArXiv e-prints*.
- 502 43. Neal RM (1996) *Bayesian Learning for Neural Networks*. (Springer).
- 503 44. Hoffman MD, Gelman A (2011) The No-U-Turn Sampler: Adaptively Setting Path Lengths in  
504 Hamiltonian Monte Carlo. *arXiv e-prints* p. arXiv:1111.4246.
- 505 45. Gelman A, Rubin DB (1992) Inference from iterative simulation using multiple sequences.  
506 *Statist. Sci.* 7(4):457–472.
- 507 46. Pourzanjani AA, Jiang RM, Petzold LR (2017) Improving the Identifiability of Neural Networks  
508 for Bayesian Inference. *NIPS Workshop on Bayesian Deep Learning*.

DRAFT